Chemical Geology 559 (2021) 119901

Contents lists available at ScienceDirect

Chemical Geology

journal homepage: www.elsevier.com/locate/chemgeo

# Fe(II)-induced transformation of iron minerals in soil ferromanganese nodules

Chengshuai Liu[a,b], Michael S. Massey[c], Drew E. Latta[d], Yafei Xia[a], Fangbai Li[b,e,*], Ting Gao[a], Jian Hua[b,e]

[a] State Key Laboratory of Environmental Geochemistry, Institute of Geochemistry, Chinese Academy of Sciences, Guiyang 550081, China
[b] Guangdong Key Laboratory of Integrated Agro-environmental Pollution Control and Management, Guangdong Institute of Eco-Environmental Sciences & Technology, Guangzhou 510650, China
[c] Department of Earth and Environmental Sciences, California State University, East Bay, Hayward, CA 94542, United States
[d] Civil and Environmental Engineering, The University of Iowa, Iowa City, IA 52242, United States
[e] National-Regional Joint Engineering Research Center for Soil Pollution Control and Remediation in South China, Guangzhou 510650, China

ARTICLE INFO

Editor: Hailiang Dong

*Keywords:*
Mineral recrystallization
Iron oxides
Soil iron cycle
Iron atom exchange
Goethite

ABSTRACT

Recrystallization of iron (hydr)oxides by ferrous iron [Fe(II)] is an important part of the biogeochemical cycling of iron in earth surface environments. Ferromanganese nodules are complex assemblages of natural Fe and Mn minerals, which are widely found in soils and marine environments, and critically impact the geochemical behavior of trace metals and nutrients. However, little is known regarding the Fe(II)-induced recrystallization of ferromanganese nodules, in comparison to pure iron (hydr)oxides. Accordingly, the objective of this study was to elucidate the reaction processes of aqueous Fe(II) with ferromanganese nodules, and to use complementary spectroscopic techniques to characterize the products. Goethite in the nodule that underwent phase transformation to magnetite or Fe(II) oxidation to form magnetite has not been reported in previous studies with respect to pure goethite. $^{57}$Fe-enriched isotope tracer experiments confirmed Fe atom exchange between aqueous Fe(II) and structural Fe(III) of the nodule and was enhanced at higher pH conditions. The coexistence of Mn oxides and other minerals possibly make the goethite in the nodule more reactive for phase transformation to magnetite than pure synthetic goethite. In addition, Fe(III) precipitates were formed due to Fe(II) oxidation by Mn(III) of the nodule, and magnetite was likely consequently produced through further Fe(II)-induced reaction. Considering the enrichment of trace metals and nutrients in ferromanganese nodules, the observed Fe(II)-induced recrystallization of nodules in the study is expected to exert important effects on the geochemical behavior of the elements, especially in nodule-enriched soils.

## 1. Introduction

Ferromanganese nodules are common components in soils exhibiting imperfect drainage or limited permeability, and are formed under seasonal changes in the soils' redox potential (Eh) and pH (Jien et al., 2010; Yu et al., 2015). Soil ferromanganese nodules are composed of primary and secondary minerals such as quartz, K-feldspars, plagioclases, and clay minerals, which are cemented together with iron and manganese oxides (Szymański et al., 2014; Milad and Taymor, 2017). Ferromanganese nodules are of great significance in environmental geochemistry because of their strong adsorption and enrichment of many elements including toxic metal pollutants (Manceau et al., 2003; Manceau et al., 2007), rare earth metals (Marcus et al., 2018), and plant nutrients (Huang et al., 2009; Jien et al., 2010). For example, the averages of K, Na, Co, and Pb concentrations in ferromanganese nodules are about 2.0, 1.4, 15.4, and 6.0 times higher, respectively, than those in Alfisols from central China (Huang et al., 2009). Therefore, in the past, most of the studies for soil ferromanganese nodules concentrated on the accumulation of metals in this stable carrier mineral (Chao, 1972; Langlois and James, 2015; Timofeeva, 2008;

* Corresponding author at: Guangdong Key Laboratory of Integrated Agro-environmental Pollution Control and Management, Guangdong Institute of Eco-Environmental Sciences & Technology, Guangzhou 510650, China.
*E-mail address:* cefbli@soil.gd.cn (F. Li).

https://doi.org/10.1016/j.chemgeo.2020.119901
Received 31 January 2020; Received in revised form 18 September 2020; Accepted 20 September 2020
Available online 25 September 2020

Frierdich and Catalano, 2012a; Timofeeva et al., 2014).

Siderophilous metals, e.g. Pb, Cr, Ni, and some other trace metals, e.g. Zn, are reported with ferromanganese nodules in soils (Manceau et al., 2003, 2007; Cornu et al., 2005; Huang et al., 2009; Mohwinkel et al., 2014; Chang et al., 2016). The existing form and stability of the Fe/Mn-bearing components, therefore, are crucial to understanding the geochemical behavior of the concentrated metals in soil ferromanganese nodules. Soil conditions, including the pH and Eh, microorganisms, redox-active reactants, etc., potentially affect the stability of the iron composition of the ferromanganese nodules, but few studies have investigated the structural transformation behavior of ferromanganese nodules.

The iron cycle is influenced by a suite of biogeochemical processes in soils, including dissimilatory microbial iron reduction and oxidation of ferrous iron (e.g., Weber et al., 2006; Borch et al., 2010; Roden, 2012; Chen et al., 2014). In recent years, atom exchange between the iron oxides and aqueous or sorbed Fe(II) under anoxic environments was found to be another important reaction in the iron cycle (Hansel et al., 2003, 2005; Williams and Scherer, 2004; Pedersen et al., 2005; Burton et al., 2010; Rosso et al., 2010; Handler et al., 2014; Massey et al., 2014a; Frierdich et al., 2015; Reddy et al., 2015; Jones et al., 2017; Joshi et al., 2017; Notini et al., 2018; Taylor et al., 2019). Spectroscopic studies and experiments using Fe stable isotopic tracers indicate that electron transfer and Fe atom exchange between aqueous Fe(II) ($Fe(II)_{(aq)}$) and structural Fe(III) in iron oxides ($Fe(III)_{oxide}$) occur upon adsorption of Fe ($II)_{(aq)}$ on iron oxides under anaerobic conditions (Williams and Scherer, 2004; Yanina and Rosso, 2008; Rosso et al., 2010; Gorski et al., 2012; Frierdich et al., 2019). These reactions also drive the transformation of iron oxides, often to more-crystalline forms (Hansel et al., 2003; Pedersen et al., 2005; Boland et al., 2014; Liu et al., 2016). To date, most research on Fe(II)-driven transformation of iron oxides, however, have focused on synthetic, pure iron oxides. In natural systems, most iron minerals contain impurities in their crystal structure (e.g., Cismasu et al., 2011), which tend to slow or inhibit electron transfer and Fe atom exchange (Hansel et al., 2011; Latta et al., 2012; Frierdich et al., 2012; Frierdich and Catalano, 2012b; Massey et al., 2014b).

The extent to which iron oxides can exchange atoms with $Fe(II)_{(aq)}$ is known for the pure iron minerals, e.g. goethite (Handler et al., 2009), magnetite (Gorski et al., 2012), and even hematite (Yanina and Rosso, 2008; Frierdich et al., 2015). Despite the compelling and growing body of work that closely links interaction between $Fe(II)_{(aq)}$ and $Fe(III)_{oxide}$ of synthetic iron minerals, the mineralogical transformation of natural iron minerals by $Fe(II)_{(aq)}$ remains poorly understood (Tishchenko et al., 2015). So far, to our knowledge, few works have focused on the interaction of $Fe(II)_{(aq)}$-$Fe(III)_{oxide}$ with natural soil minerals. Latta et al. (2012) investigated how electron transfer between sorbed Fe(II) and Fe ($III)_{oxide}$ was impacted by Al(III) substitution in goethite. $^{57}$Fe Mössbauer spectroscopy suggested that redox-inactive Al(III) substitution (up to 10%) did not significantly inhibit electron transfer (Latta et al., 2012). Conversely, structural redox-active Mn(III) in goethite (Frierdich and Catalano, 2012c) and Mn(IV) in pyrolusite (β-$MnO_2$) are reduced to Mn(II) by $Fe(II)_{(aq)}$ resulting in the formation of the iron (hydr)oxides, including lepidocrocite and magnetite (Schaefer et al., 2017).

Although previous studies clearly indicated electron transfer and Fe atom exchange between $Fe(II)_{(aq)}$-$Fe(III)_{oxide}$ in pure iron oxides, the Fe (II)-induced phase transformation of natural, impure iron oxides has remained less clear, especially for complex, iron-rich soil solids like ferromanganese nodules. The objective of this study is to elucidate the reaction of aqueous $Fe(II)_{(aq)}$ with ferromanganese nodules. Quantitative X-ray diffraction (QXRD) was used to assess the possibility and rates of phase transformation of the iron components in ferromanganese nodules, and Mössbauer spectroscopy was used to explore electron transfer between $Fe(II)_{(aq)}$-$Fe(III)_{oxide}$ in ferromanganese nodules. Additionally, Fe atom exchange processes between $Fe(II)_{(aq)}$ and ferromanganese nodules under different conditions were monitored with an enriched isotope tracer $^{57}$Fe approach.

## 2. Materials and methods

### 2.1. Sampling and characterization of the ferromanganese nodules

Ferromanganese nodules were collected from the subsurface soil (20 cm to 40 cm) in a paddy soil in Laibin City, Guangxi Province, China (23°42′ N, 109°38′ E). The nodule-enriched soils were oven dried at 60 °C, and soil and nodules were manually separated. Nodules were immersed into distilled water and sonicated for 1 min to remove clinging soil particles from the nodule surfaces; the washing step was repeated three times to obtain relatively clean ferromanganese nodules. Clean nodule particles with an approximate diameter of ~2 mm were selected randomly, and ground together to pass through an 80-mesh sieve. The resulting sieved powders were collected for subsequent analyses and experiments. The phase compositions of the powders were characterized with Quantitative X-ray diffraction (QXRD) (the method details are provided in Section 2.4).

### 2.2. Fe(II) sorption experiments

All batch experiments were carried out in an anaerobic glovebox (96% $N_2$, 4% $H_2$) with $O_2$ maintained at <1 ppm by continual atmospheric circulation over a Pd catalyst. The solutions prepared outside the anaerobic glovebox were purged with $N_2$ for at least 2 h $L^{-1}$ and then covered tightly prior to transferring into the glovebox. Solutions were then opened to equilibrate inside the glovebox for 24 h or longer and the anaerobic condition was confirmed through dissolved oxygen meter. The 100 mM stock solutions of Fe(II) with natural Fe isotopic abundance were obtained by dissolving $FeCl_2{\cdot}4H_2O$ in deionized water in the glovebox.

Variable Fe(II) sorption experiments were conducted in the glovebox in triplicate reactors (15 mL centrifuge tubes were used as reactors). Each reactor contained 0.03 g $L^{-1}$ ferromanganese nodule powder and 15 ± 0.02 mL Fe(II) solution ranging from 0 to 2.5 mM, in a background electrolyte with 25 mM HEPES (4-(2-hydroxyethyl)-1-piperazineethanesulfonic acid) and 25 mM KBr, at the pH of 7.5 (detailed procedure can be found in the Supporting information, SI, text S1). The reactors were sealed with an O-ring and Teflon tape before being tightly capped, wrapped in Al foil, and placed on an end-over-end rotator at room temperature. Sorption equilibrium was reached within 24 h based on a preliminary test (not shown). After 24 h, the reactors were centrifuged outside the glovebox at ~6500 rpm for 5 min, and immediately returned to the glovebox. The supernatant was decanted off the pelleted solid, and filtered through a 0.22 μm hydrophilic PTFE filter (Millipore, MA, USA). After acidification with 50 μL concentrated HCl, the solution was transferred outside of the glovebox for Fe(II) analysis using the ferrozine method (Stookey, 1970).

After decanting the supernatant, 0.4 M HCl was used to extract sorbed Fe(II) on the surface of the reacted nodules (Frierdich et al., 2014a). After extraction with HCl for 10 min, the suspension was centrifuged and the supernatant was analyzed for Fe(II) and total Fe concentration, again using the ferrozine method. The HCl extractant supernatant was decanted, and the residual solids were further digested using a modified $HNO_3$-HF-$HNO_3$ method (Naskar et al., 2016) (details for the digestion are provided in SI, text S2). After digestion of the residual solids, these solutions were measured to determine the total Fe (II) and Fe(III) concentrations.

Similarly, variable-pH Fe(II) sorption experiments were conducted on the nodule material at different pH values (pH 3.0, 5.5, 6.0, 6.5, 7.0, and 7.5). The same experimental procedures were used, except: (i) In all reactors, the amount of nodule and Fe(II) concentration were fixed at 0.03 g $L^{-1}$ and 1.0 mM, respectively; (ii) The pH of the suspensions in the reactors were adjusted to the desired pH values with 0.1 M HCl or KOH after being buffered with 25 mM of PIPPS (piperazine-*N*,*N*′-bis(2-propanesulfonic acid)) (pH 3.0), MES (2-(N-morpholino) ethanesulfonic acid) (pH 5.5, 6.0, and 6.5), or HEPES (pH 7.0 and 7.5) The pH was

monitored and remained constant (< 0.02 units drift) throughout the experiments.

### 2.3. Experiments of Fe isotope exchange and phase transformation

A stock solution of $^{57}$Fe(II) was prepared inside the glovebox by dissolving enriched $^{57}$Fe isotope (>95%) metal (Isoflex, San Francisco, CA, USA) under magnetic stirring at about 60 °C overnight. Isotope exchange experiments between $^{57}$Fe(II)-spiked solutions and the nodule were carried out under similar conditions as the Fe(II)-induced reaction experiments (Section 2.2). In each reactor, an aliquot of the $^{57}$Fe(II) solution was added to give an approximate concentration of 1 mM $^{57}$Fe $(II)_{(aq)}$ in 15 mL of 25 mM HEPES buffer containing 25 mM KBr, and the pH was adjusted back to a value of 7.5 with 0.1 M KOH. Initial solution samples were withdrawn at this point for analyses of the initial aqueous Fe isotope composition and $Fe(II)_{(aq)}$ concentration. Then, 0.03 g $L^{-1}$ of nodule powder was added to initiate the reaction.

At specific time intervals ranging from 1 day to 30 days, triplicate reactors were selected for sampling and transferred outside of the glovebox for separation by centrifuge at ~6500*g* for 5 min. After centrifuging, the reactors were immediately returned to the glovebox. The supernatant was decanted off the pelleted nodule material, and filtered through a syringe filter membrane (0.22 μm, nylon), and acidified with 50 μL concentrated HCl. The remaining nodule pellets were used to analyze Fe isotope composition (see SI, text S3) and Fe concentrations after being digested with the $HNO_3$-HF-$HNO_3$ method, or to characterize the mineral compositions with X-ray diffraction (XRD) after being air-dried in the glovebox.

To further explore the phase transformation of iron oxides in the nodule, the experiments reacting the nodule with $^{56}$Fe-enriched Fe(II) solution were conducted using the procedures outlined above. The $^{56}$Fe (II) stock solution was prepared inside the glovebox by dissolving $^{56}$Fe-enriched (>99.9%) metal with the same method as in the preparation of $^{57}$Fe(II) stock solution. After reaction, the residual solids were collected on the filter membrane (0.22 μm, nylon) by filtering the suspension of one reactor. The homogenously-distributed thin paste of reacted nodule on the membrane was partially dried under nitrogen (~4 min), then sealed between two pieces of Kapton polyimide film and transferred outside of the glovebox for Mössbauer analysis.

### 2.4. Solid phase analyses using crystallographic and spectroscopic methods

Fe(II)-induced phase transformations were monitored using powder X-ray diffraction (XRD). Diffraction patterns of each solid sample were recorded by a Bruker D8 ADVANCE X-ray powder diffractometer equipped with a Lynx Eye detector and Ni-filtered Cu *Kα* X-ray source (λ = 0.154 nm, 40 kV, 40 mA). The 2*θ* scanning range was 10–90°, and the step size was 0.02° with a scan time of 1 s per step. Phase identification was carried out by matching the obtained XRD patterns with the standard powder diffraction database (International Centre for Diffraction Data ICDD PDF-2, Release 2008) (Lu et al., 2013). Quantitative analyses of the relative abundance of different phases in each sample were obtained using two-phase Rietveld quantitative analysis of the XRD patterns in the GSAS software program (Toby, 2001).

Mössbauer spectra of the solids before and after reaction with $^{56}$Fe (II) were collected at 13 K on a spectrometer supplied by Web Research, Inc. (Edina, Minnesota, USA) equipped with a closed-cycle cryostat (CCS-850 System, Janis Research Co., Wilmington, Massachusetts, USA). The spectra were obtained in transmission mode with a constant acceleration drive system and a $^{57}$Co source (30–40 mCi), and the isomer shift (IS) was calculated against a 7 μm *α*-Fe(0) foil. The data were fitted using Recoil software (Ottawa, Canada) using Voigt-based fit, following the fitting procedures reported previously (Neumann et al., 2013).

The Fe *K*-edge extended X-ray absorption fine structure (EXAFS) spectra of the nodule material and synthetic goethite (for comparison, using the same synthesis method provided in Schwertamnn and Cornell, 2000) were recorded at the 17C1 Beamline of National Synchrotron Radiation Research Center (NSRRC) in Taiwan in transmission geometry. Energy calibration was ensured by comparing spectra to the absorption edge of an inline Fe metal foil, measured simultaneously with the powder samples. The first inflection point of the Fe foil spectrum was calibrated to 7111 eV.

Mn species were identified through X-ray photoelectron spectroscopy (XPS, ESCALAB 250XI, Thermo Scientific). Detailed procedures of the spectroscopic characterizations were provide as Texts S4 in SI. To probe the oxidation states of Mn in the nodule before and after reaction with $Fe(II)_{(aq)}$, X-ray absorption near-edge structure (XANES) spectra at the Mn *K*-edge were obtained at the Advanced Photon Source MR-CAT/EnviroCAT Sector 10 bending magnet beamline, Argonne National Laboratory (Chicago, Illinois, USA). Before XANES analysis of the reacted samples, 10 mL of the suspension was filtered onto 0.22 μm filter membranes, mounted between layers of Kapton film, and sealed with Kapton tape. A standard of 100 mM $MnCl_2$ dissolved in deionized water was sealed in a drilled plastic holder between layers of Kapton film. Mineral standards of bixbyite ($Mn_2O_3$) and pyrolusite ($MnO_2$) were ground and spread as a thin adherent layer on Kapton tape and folded to achieve an acceptable XANES signal (e.g. edge step between 0.2 and 0.7). Energy calibration of the Mn *K*-edge spectra was achieved by comparison to a Mn foil with a first inflection point at 6539 eV. Mn *K*-edge spectra of unknown samples and foil were measured simultaneously, with foil and mineral standard data collected in transmission geometry, and sample data and aqueous Mn(II) data collected in fluorescence geometry. Analyses of the Mn X-ray absorption spectra (XAS) spectra were performed using the Athena program (Ravel and Newville, 2005). Background subtraction and edge-step normalization were done using the Autobk algorithm with a Rbkg value of 0.9, an E0 of 6550.5 eV, a pre-edge range of −50 to −20 eV and a post-edge range of +50 to +175 eV.

## 3. Results

### 3.1. Fe(II) sorption on ferromanganese nodules

Sorption is considered as the initial and crucial step of direct interaction between $Fe(II)_{(aq)}$ and the solids (Reddy et al., 2015; Liu et al., 2016). The sorption of $Fe(II)_{(aq)}$ (extracted with 0.4 M HCl) on the nodule material was investigated under different conditions. A set of sorption experiments with varying initial $Fe(II)_{(aq)}$ concentrations (0.25 to 2.6 mM) were carried out to determine the sorption isotherm of Fe (II) on powdered nodule material (2.0 g $L^{-1}$) at pH 7.5 (Fig. 1A). The sorption reactions reached equilibrium within 24 h (not shown). With an initial $Fe(II)_{(aq)}$ concentration of 0.25 mM, approximately 1.53 μmol of Fe(II) in the system (41.5% of the total Fe(II)) was sorbed to the solid, while at a $Fe(II)_{(aq)}$ concentration of 2.6 mM, 4.67 μmol of Fe(II) in the system (11.9% of the total Fe(II)) was sorbed to the solid. Though additional $Fe(II)_{(aq)}$ did not sorb to the solid at concentrations higher than ~1.5 mM, variation in Fe(II) concentration may have altered the resulting reaction products, likely green rust, lepidocrocite, goethite, and magnetite, as has been observed in similar systems (e.g., Hansel et al., 2005).

Fe(II) sorption on the nodule at different pH conditions was also investigated and the results are provided in Fig. 1B. The amounts of sorbed Fe(II) on the nodule accordingly increased with raised pH. At a pH of 3.0, no sorption of Fe(II) on the nodule material was observed. At pH 5.5 however, 0.92 μmol of Fe(II) (6.1% of the total Fe(II)) was sorbed after 24 h. The amount of sorbed Fe(II) increased substantially at higher pH (> 5.5), with as much as 8.89 μmol (59.3% of the total Fe (II)) of sorbed Fe(II) at pH 7.5.

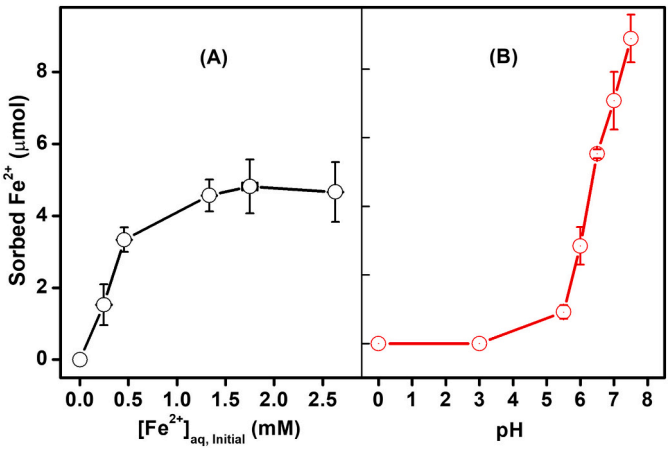


**Fig. 1.** Sorption of Fe(II)$_{(aq)}$ on the ferromanganese nodule at room temperature: (A) adsorption isotherm of Fe(II) on the nodule (2.0 g $L^{-1}$) at pH 7.5 with different initial concentrations of Fe(II); (B) adsorbed amounts of Fe(II) on the nodule (2.0 g $L^{-1}$) at varying pH with the initial concentration of Fe(II) at 1.0 mM. Values for data points represent the mean of triplicate reactions; errors bars not visible are smaller than symbols.

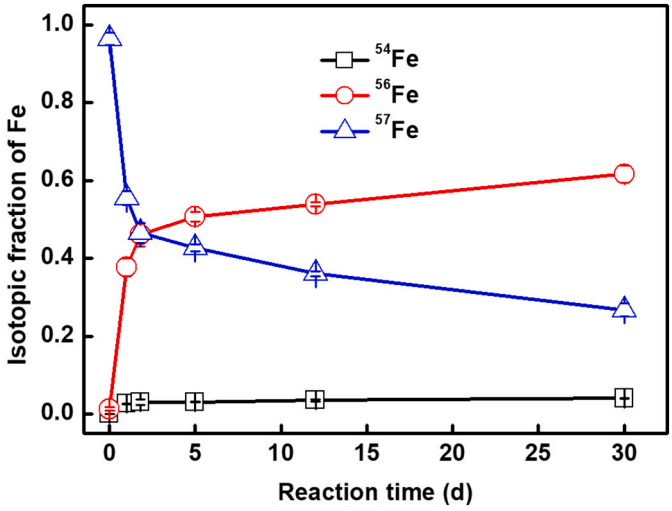


**Fig. 2.** Temporal evolution of the iron isotope fractions (Eq S1 in SI) of Fe(II)$_{(aq)}$ (1.0 mM) during its reaction with the ferromanganese nodule (2.0 g $L^{-1}$) at pH 7.5 buffered by 25 mM HEPES/KBr. Fe(II)$_{(aq)}$ was initially enriched in $^{57}$Fe (0.96), and the nodule initially has a natural-abundance iron isotope composition (0.02, 0.92, and 0.05 for $^{57}$Fe, $^{56}$Fe, and $^{54}$Fe, respectively).

### 3.2. Fe atom exchange between Fe(II)$_{(aq)}$ and Fe(III)$_{oxide}$ of the ferromanganese nodule

To probe the extent and rate of Fe atom exchange between Fe(II)$_{(aq)}$ and Fe(III)$_{oxide}$ in the nodule, we conducted a $^{57}$Fe-enriched isotope tracer experiment adapting an approach similar to that used in previous studies (Gorski et al., 2012; Latta et al., 2012; Frierdich et al., 2015; Neumann et al., 2015; Liu et al., 2017). We reacted isotopically naturally abundant nodule material with a 1 mM $^{57}$Fe-enriched Fe(II)$_{(aq)}$ solution buffered at different pH values. By measuring the changes of isotopic composition in both Fe(II)$_{(aq)}$ and the nodule over time, we could track the Fe atom exchange between Fe(II)$_{(aq)}$ and Fe(III)$_{oxide}$ in the nodule, in which $^{57}$Fe atoms move from the aqueous phase into the nodule structure, and isotopically naturally abundant Fe atoms from the nodule into the aqueous phase. The initial Fe isotope composition of Fe(II)$_{(aq)}$ was almost entirely $^{57}$Fe ($f^{57}$Fe = 0.965 in Table 1). After initiating the reaction at pH 7.5, the fraction of $^{57}$Fe in Fe(II)$_{(aq)}$ began to decrease, whereas the fractions of $^{56}$Fe and $^{54}$Fe in the aqueous phase increased (Fig. 2); the changing isotopic composition clearly indicates that $^{57}$Fe-enriched Fe(II) exchanged with the Fe in the nodule.

Calculations of Fe exchange percents in the nodule with Fe(II), via $f^{57}$Fe of Fe(II)$_{(aq)}$, were conducted by using a mass balance approach as discussed previously (Handler et al., 2014; Frierdich et al., 2015):

$$\%\text{Fe exchange} = \frac{N_{aq} \times (f_{aq}^{i} - f_{Fe(II)}^{t})}{N_{Nod}^{tot} \times (f_{Fe(II)}^{t} - f_{Nod}^{ti})} \times 100 \quad (1)$$

where $N_{aq}$ is the total number of Fe(II) in the aqueous solution, $N_{Nod}{}^{Tot}$ is the total number of structural Fe in the nodule, $f_{aq}{}^{i}$ represents the initial isotope composition of Fe(II)$_{(aq)}$, $f_{Fe(II)}{}^{t}$ represents the Fe isotopic composition of Fe(II) at each time point $t$, and $f_{Nod}{}^{i}$ represents the initial isotope composition of Fe(III) in the nodule. As reported previously, we used the isotopic composition of Fe(II)$_{(aq)}$ as an easily accessible tracer for estimating the extent of Fe atom exchange here, and did not consider a comprehensive mass balance approach for all Fe(II) species.

As estimated, Fe atom exchange occurred under the studied three different pH conditions (Table 1, Fig. 3). After 1 day, 1.9% of the Fe atoms in the nodule exchanged with Fe(II) at pH 3.0, and Fe atom exchange increased to 3.6% and 6.2% at pH 5.5 and 7.5, respectively. The extent of Fe atom exchange increased with time, to 3.6%, 6.10%, and 21.5% at the pH conditions of 3.0, 5.5, and 7.5, respectively, after a reaction time of 30 days. In all cases, higher Fe atom exchange was observed at higher pH values.

**Table 1**
Mass and isotope data for Fe isotope tracer experiments between aqueous Fe(II) and structural Fe of the nodule at different reaction pH.

| | Time (days) | $Fe_{(aq)}$ (μmol) | $f^{57}$Fe | $Fe_{nodule}$ (μmol) | $f^{57}$Fe | Exchange $^{57}Fe_{(aq)}$ (%) |
|---|---|---|---|---|---|---|
| pH 7.5 | 0.01 | 16.5 (0.85)[a] | 0.965 (0.004) | 209.2 (9.5) | 0.024 (0.0002) | 0 |
| | 1 | 10.7 (0.70) | 0.553 (0.079) | 205.0 (13.9) | 0.033 (0.0013) | 6.2 (0.5) |
| | 1.79 | 7.6 (0.22) | 0.454 (0.042) | 209.5 (15.8) | 0.039 (0.0045) | 9.4 (1.0) |
| | 5 | 9.19 (0.48) | 0.428 (0.085) | 205.4 (15.9) | 0.058 (0.0029) | 10.5 (0.7) |
| | 12 | 5.7 (0.35) | 0.366 (0.007) | 208.9 (13.9) | 0.060 (0.0062) | 13.8 (1.2) |
| | 30 | 6.42 (0.68) | 0.277 (0.074) | 207.8 (22.5) | 0.073 (0.0093) | 21.5 (1.0) |
| pH 5.5 | 0.01 | 16.3 (0.31) | 0.965 (0.004) | 209.2 (9.5) | 0.024 (0.0002) | 0 |
| | 1 | 15.4 (0.20) | 0.668 (0.074) | 200.4 (14.9) | 0.029 (0.0008) | 3.6 (0.3) |
| | 5 | 14.4 (0.22) | 0.611 (0.103) | 180.9 (19.6) | 0.034 (0.0010) | 4.8 (0.6) |
| | 30 | 15.0 (0.22) | 0.557 (0.118) | 178.5 (22.8) | 0.039 (0.0116) | 6.1 (0.5) |
| pH 3.0 | 0.01 | 16.3 (0.50) | 0.965 (0.004) | 209.2 (9.5) | 0.024 (0.0002) | 0 |
| | 1 | 16.4 (0.22) | 0.784 (0.009) | 168.2 (18.4) | 0.027 (0.0006) | 1.9 (0.2) |
| | 5 | 16.4 (0.12) | 0.752 (0.069) | 166.8 (20.1) | 0.027 (0.0007) | 2.3 (0.4) |
| | 30 | 15.8 (0.11) | 0.670 (0.057) | 163.3 (23.4) | 0.028 (0.0006) | 3.6 (0.3) |

[a] The numbers in the brackets are the standard deviations from triplicate samples.

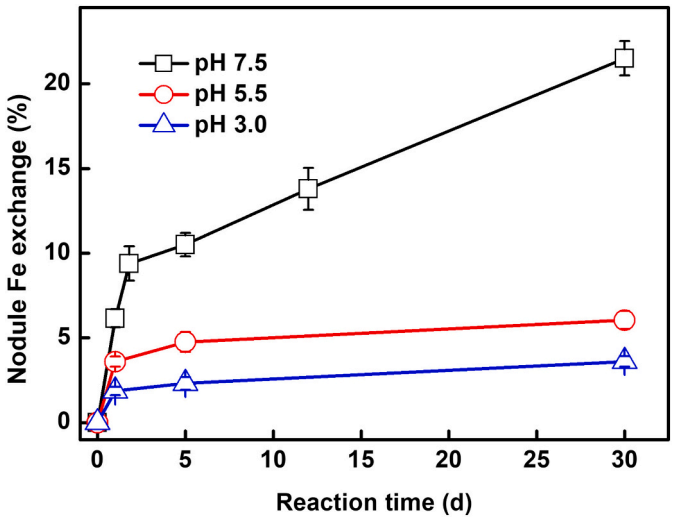


**Fig. 3.** Extent of Fe isotope exchange between Fe(II)$_{(aq)}$ and structural Fe in the nodule at different reaction pH. The extent of Fe atom exchange was calculated from aqueous phase $^{57}$Fe with Eq. (1) based on the measured Fe isotope fractions with the quadrupole ICP-MS. Values for data points represent the mean of triplicate reactions; errors bars not visible are smaller than symbols.

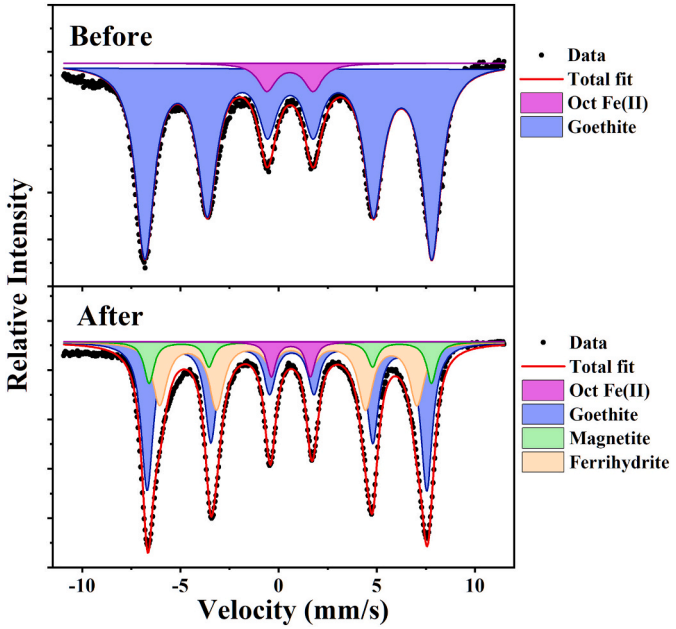


**Fig. 5.** The $^{57}$Fe Mössbauer spectra of isotopically naturally abundant nodule (1.0 mM) at 13 K before and after anoxic reaction with 1.0 mM $^{56}$Fe(II)$_{(aq)}$ at pH 7.5 for 30 days.

### *3.3. Phase characterization of the nodule material during Fe(II)-induced reaction*

To evaluate Fe(II)-induced phase transformations of iron minerals in the nodule material, we reacted the nodule material with a 1 mM Fe (II)$_{(aq)}$ solution buffered at pH 7.5, and quantified the relative intensities of the different crystalline mineral constituents in the nodule material based on XRD data using Rietveld refinement (Fig. 4). The main crystalline minerals in the pristine ferromanganese nodule powder were goethite (77.6%), kaolinite (16.4%), rutile (2.6%), manganite (1.7%), quartz (1.5%), and cryptomelane (0.2%). After reacting the nodule with Fe(II), goethite decreased to 54.9% after 2 days, and continued to decline further, to 20.7% after 30 days (Fig. 4B). Magnetite was identified with a content of 30.1% after 2 days of reaction, which further increased to 73.2% after 30 days. Two Mn-bearing crystallines, i.e. manganite and cryptomelane, were identified in the nodule. The percentage of manganite decreased to 0.3% at 30 days while cryptomelane did not show obvious change. Resulting from the dilution by the newly formed phases (i.e. magnetite), the percentage of quartz and other non-reactive crystalline components declined.

Mössbauer spectroscopy was also employed to characterize the changes of structural $^{57}$Fe in the isotopically naturally abundant nodule after reaction with $^{56}$Fe-enriched Fe(II)$_{(aq)}$. Mössbauer spectroscopy only detects $^{57}$Fe among all the four stable iron isotopes and the other three stable iron isotopes ($^{54}$Fe, $^{56}$Fe, and $^{58}$Fe) are transparent and invisible by Mössbauer spectroscopy, which allows for the observation of the changes to structural $^{57}$Fe in the nodule after reaction with $^{56}$Fe (II) (Williams and Scherer, 2004). In comparison with the quantitative XRD, Mössbauer spectrum is of higher sensitivity facilitating the quantification of the low-content and amorphous iron (hydr)oxides in the solids. The $^{57}$Fe Mössbauer spectra at 13 K of isotopically naturally abundant nodule material before and after reaction with aqueous $^{56}$Fe (II) are shown in Fig. 5 and Table S1. The spectra before reaction clearly indicated the iron components in the nodule included crystalline goethite and Fe(II) in the nodule, which is consistent with the large amount of the goethite phase identified by the XRD results. The fitting results from the Mössbauer spectra before and after reaction with $^{56}$Fe(II) also suggested that, besides the goethite (isomer shift (IS) = 0.54 mm/s, quadrupole splitting (QS) = −0.22 mm/s), magnetite (IS = 0.61 mm/s, QS = -0.02 mm/s) and ferrihydrite (IS = 0.56 mm/s, QS = -

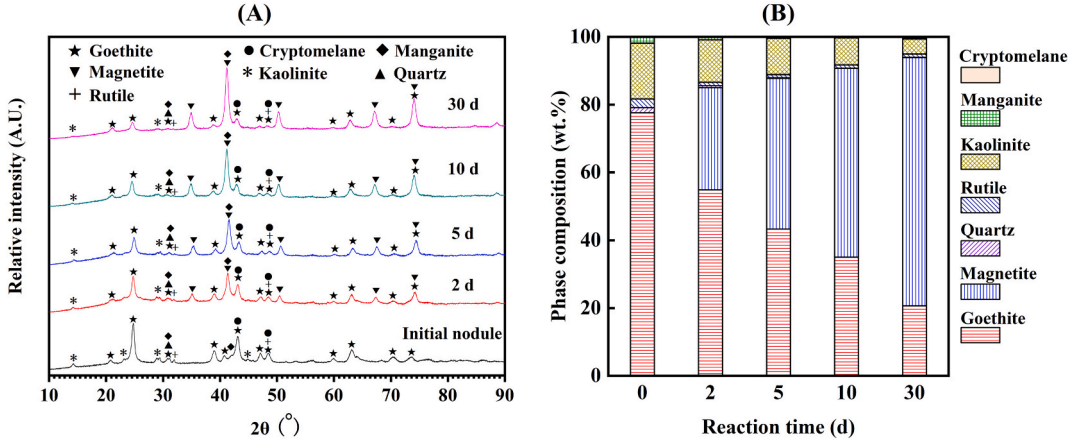


**Fig. 4.** The XRD patterns of the nodule (2.0 g L$^{-1}$) after reacting with Fe(II)$_{(aq)}$ (1.0 mM) anaerobically at pH 7.5 for different times (A), and the corresponding calculated phase compositions of different minerals in the nodule based on the XRD results (B).

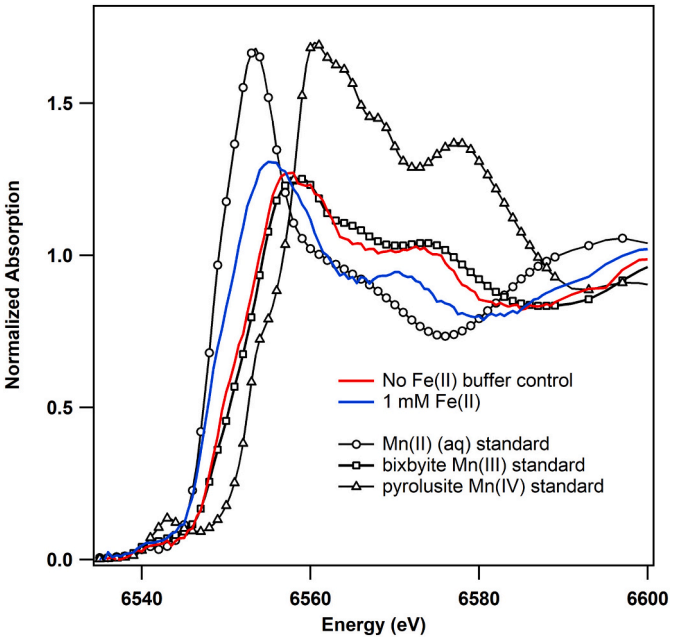


**Fig. 6.** Manganese *K*-edge X-ray absorption near edge spectra (XANES) of the nodule after 30 days without (red) and with (blue) reaction with 1.0 mM Fe $(II)_{(aq)}$. Reference spectra for comparison are $Mn(II)_{(aq)}$ as a 100 mM $MnCl_2$ solution, Mn(III) as $Mn_2O_3$ (bixbyite), and Mn(IV) as $MnO_2$ (pyrolusite). (For interpretation of the references to color in this figure legend, the reader is referred to the web version of this article.)

0.13 mm/s) also appeared after reaction. XRD only detected the crystalline magnetite without the amorphous ferrihydrite in the products.

### 3.4. Mn species of the nodule material during Fe(II)-induced reaction

The oxidation state of Mn was investigated to identify its involvement to the Fe(II)-induced reaction. As shown by the Mn *K*-edge XANES results (Fig. 6), the spectrum of the pristine ferromanganese nodule was similar to that of the Mn(III) standard. This is consistent with the XPS result (Fig. S1) that the majority of the Mn-bearing components in the nodule was Mn(III) with small proportion of Mn(II) and Mn(IV). Besides the identified crystalline phases of manganite [Mn(III)] and cryptomelane [Mn(IV)] (Fig. 4), the nodules may contain amorphous Mn(II) and Mn(III) which could not be detected by XRD.

According to the XANES result (Fig. 6), the spectrum showed an obvious shift to a lower energy after reaction with Fe(II), which became closer to the spectrum of the Mn(II) standard. The shift in the XANES suggests that the oxidation state of the Mn-bearing components in the nodule was reduced, likely through reaction with Fe(II).

## 4. Discussion

### 4.1. Fe(II) sorption behavior by the ferromanganese nodule

We investigated the sorption behavior of Fe(II) on ferromanganese nodule in order to uncover the first step of the interaction of Fe(II) and ferromanganese nodule. The initial sorption step in Fe(II)-mineral interactions is usually crucial for subsequent reactions (Reddy et al., 2015; Liu et al., 2016). Our results indicate the effective sorption of Fe (II) on the ferromanganese nodule. Additionally, consistent with previous results regarding Fe(II) sorption on synthetic pure iron minerals, e.g. goethite (Reddy et al., 2015) and hematite (Frierdich et al., 2015), sorption of $Fe(II)_{(aq)}$ on the nodule was highly dependent on pH (Fig. 1B). This behavior is consistent with the general adsorption behavior of metal cations that form inner-sphere sorption complexes with mineral surface functional groups such as hydroxyls: at low pH, the surface functional groups and hydrated metal complexes in solution do not favor adsorption for most metal cations. Sorption behavior of Fe(II) and many other metal cations is defined by this characteristic adsorption edge, related to hydrolysis species in solution. Not coincidentally, $[Fe(OH)]^+$ becomes the dominant Fe(II) solution complex at around pH 6.75 (Lindsay, 1979), which leads to the Fe(II) facilely adsorbed on the minerals. Chemically-dominated sorption of Fe(II) is consistent with observed behavior of Fe(II) on hematite (e.g., Jeon et al., 2001) and goethite (e.g., Reddy et al., 2015). However, in the case of Fe(II), adsorption is but the initial step in a much broader suite of reactions and processes such as redox reactions, electron transfer, bulk conduction of electrons, and mineral transformation.

Each component in the natural ferromanganese nodule materials, including iron oxides, manganese oxides, and other non-Fe/Mn components like quartz or kaolinite, contributes to the physical and chemical properties, which would make them different from synthetic iron oxides. Thus, there are some different sorption results of $Fe(II)_{(aq)}$ on the nodule material, versus synthetic oxides. The differences in surface functional groups may contribute to altered sorption behavior. For example, Reddy et al. (2015) reported little sorption of Fe(II) at a pH of 2.5 with goethite, whereas in the present experiment, no sorption was observed with the nodule material at pH 3.0. Furthermore, reduction of Mn(III) or Mn(IV) by Fe(II) may increase the uptake of Fe(II). Mineralogical heterogeneity in the ferromanganese nodules contributed to the differences in Fe(II) sorption behavior. The co-existing minerals like kaolinite and Mn oxides generally have a lower point of zero charge (PZC) than iron oxides such as goethite, which has a PZC of pH 7.0–8.5 (Scroth and Sposito, 1997; Kosmulski, 2001). Thus the ferromanganese nodule material's PZC of pH 5.2 is lower than that of the pure goethite, which is beneficial for the metal cation sorption. In ferromanganese nodules, Mn oxides are reportedly the main scavengers of metal cations (Tan et al., 2005). The large adsorptive capacity and reactive surface of Mn oxides may contribute to Fe(II) adsorption. Besides, ligand exchange and bridge formation facilitates the sorption behavior (Casey, 2001; Handler et al., 2014). Compared with pure goethite, the complicated mineral composition of the ferromanganese nodule may change the deprotonation of oxygen atom, which would then influence the ligand exchange and bridge formation, further leading to differed Fe (II) sorption behavior. Differences in surface functional group behavior between pure iron oxides and ferromanganese nodules can be invoked to explain subtle differences in Fe(II) sorption behavior.

### 4.2. The possibility and efficiency of Fe atom exchange in the ferromanganese nodule

Fe atom exchange was investigated as the key step that impacts the interplay between $Fe(II)_{(aq)}$ and the ferromanganese nodule. The results of $^{57}Fe$ tracing analysis (Fig. 2) indicate efficient Fe atom exchange between $Fe(II)_{(aq)}$ and $Fe(III)_{oxide}$ of the nodule. The $^{56}Fe(II)$ that was incorporated into the nodule material then formed magnetite or goethite though the atom exchange and phase transformation, while the $^{56}Fe$ oxides were invisible in the Mössbauer data. Similar Fe atom exchange has been observed between Fe(II) and synthetic pure Fe (hydr) oxides (Handler et al., 2009; Frierdich et al., 2014a, 2014b, 2015; Taylor et al., 2019), cations substituted Fe (hydr)oxides (Latta et al., 2012; Frierdich et al., 2012), and Fe-minerals in the presence of organic matter (ThomasArrigo et al., 2017; Zhou et al., 2018). However, Fe mobility into and out of natural iron minerals, especially in mixed mineral solids such as the nodule, has not been previously observed. One potential reason for this is that mixed minerals are typically regarded as structurally more stable and sterically “protected” than Fe (hydr)oxides (Tishchenko et al., 2015). That is, chemical heterogeneity and impurities can be impediments to chemical reactions. For example, substitution of Al for Fe in Fe (hydr)oxides may impede mineral transformation (Frierdich et al., 2012), which will be further discussed

in Section 4.3. In some situations, however, the presence of impurities may preserve the phase transformation of Fe (hydr)oxide, as observed by Jones et al. (2009) for Si-ferrihydrite coprecipitates.

The Fe atom exchange rates between $Fe(II)_{(aq)}$ and $Fe(III)_{oxide}$ of the nodule increased with elevated pH values, which was consistent with Fe exchange in synthetic goethite (Reddy et al., 2015) and hematite (Frierdich et al., 2015). The increased Fe atom exchange was likely due to an increase in Fe sorption at higher reaction pH. As discussed in the two references, increased amounts of sorbed Fe(II) on the nodule at higher pH conditions (Fig. 1) enhanced the direct contact of Fe(II) with goethite component in the nodule, and accordingly accelerated the Fe atom exchange.

### *4.3. Fe(II)-induced phase transformation of iron mineral component in the ferromanganese nodule material*

Iron mineral composition in the nodule was identified to trace the pathways of Fe(II)-induced transformation of ferromanganese nodules. The formation of magnetite (Fig. 4A) and its continually increased composition ratio (Fig. 4B) during the Fe(II)-induced phase transformation of the ferromanganese nodule are the most interesting results for this complex assemblages of Fe and Mn mineral in the present study. Many investigators have shown that sorbed Fe(II) can cause recrystallization of some iron minerals, which undergo transformations to other minerals (e.g., the transformation of ferrihydrite to goethite, or lepidocrocite to magnetite). More stable iron oxides, such as goethite and hematite, do not undergo transformation to other phases of iron oxides in the presence of Fe(II) (e.g., Tamaura et al., 1983; Hansel et al., 2003; Pedersen et al., 2005; Yang et al., 2010). Actually, Fe atom exchange, Fe(II)-induced recrystallization, and the formation of different iron minerals are often highly dependent on environmental conditions. For example, no Fe atom exchange between $Fe(II)_{(aq)}$ and hematite at a relatively low pH of 6.5 was reported by Pedersen et al. (2005), whereas significant Fe atom exchange between $Fe(II)_{(aq)}$ and hematite were observed at pH 8.0 by Frierdich et al. (2015). The differences in the results were ascribed to the differences in experimental conditions, e.g. smaller hematite particle size, greater surface area, and a relatively higher reaction pH (Frierdich et al., 2015). Differences in the solid phase can also significantly impact reaction products. For example, Al substitution for Fe(III) in the initial iron oxide mineral can decrease the extent of transformation (e.g., Massey et al., 2014a), or lead to different reaction products (e.g., Hansel et al., 2011; Masue-Slowey et al., 2011). As the goethite in ferromanganese nodules differs from the synthetic pure goethite in physiochemical properties and environmental reactivity, complex interactions between Fe and other important components in the nodule, e.g. manganese oxides (Frierdich and Catalano, 2012a), may have led to different mineral transformation products in this system.

As shown by the Mn *K*-edge XANES results (Fig. 6), Mn in the nodule [mostly as Mn(III)] was reduced from Mn(III) to Mn(II) by Fe(II). The resulting Fe(III) may have formed ferrihydrite or other Fe (hydr) oxide species that could subsequently form or be transformed into magnetite as reported previously (Schaefer et al., 2017). The formation of Mn(II) may also have created conditions of higher reduction potential favoring the growth of magnetite (Cheng et al., 2015).

Compared with pure goethite, the goethite in the ferromanganese nodule presumably has different physicochemical properties, whether from interactions with coexisting mineral components (i.e., kaolinite, quartz, rutile, and cryptomelane), or from impurities which might affect the goethite crystal structure. The Fourier-transformed Fe *K*-edge EXAFS spectrum showed some differences between the nodule material and synthetic pure goethite (Fig. 7). The first Fe-O interatomic distance of pure goethite was similar to that of the nodule, although the goethite was one of several co-existing Fe-bearing mineral components in the nodule. However, the Fe-Me (Me represents metals, such as Fe or other trace components) interatomic distances corresponding to second-

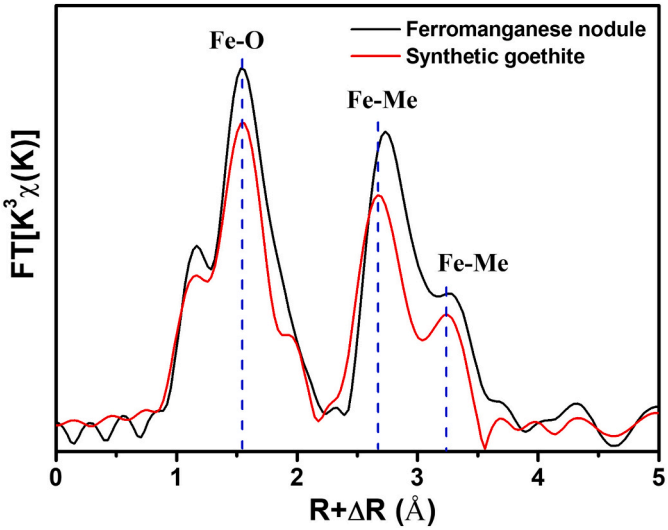


**Fig. 7.** The Fourier transform FT of $k^3$ weighted EXAFS spectra (Fe *K*-edge) as a radial structure function without the phase shift correction for ferromanganese nodule and synthetic goethite.

neighbor atoms in the nodule were elongated, compared to pure goethite. The altered Fe-Me interatomic distance may be a result of substitution of other metals in the goethite structure. For example, Manceau et al. (2000) found that the substitution of Ni for Fe in goethite increased Fe-Me interatomic distances. Firstly, the growing conditions of the nodule in soils are more complicated than the chemically synthesized pure goethite, and some Fe atoms in the goethite component are probably substituted by other metals such as the abundant elements of Mn and Al in nodules, during the formation process of the nodule in soils. Alternately, some of the differences are attributable to spectral contributions from Fe atoms in other components of the nodule material, or to structural disorder of the goethite in the nodule. The other components of the nodule material also have a larger-scale effect; the mixed solid can affect the goethite structure (Hanna et al., 2008), and thus the local coordination environment of Fe. In aggregate, Fe EXAFS data suggested that the differences in disorder between the nodule goethite and synthetic pure goethite affect the transformation behavior of the nodule goethite, resulting in the nodule being more susceptible to transformation of nodule goethite to magnetite in the present study. Besides the $Fe(II)_{(aq)}$ might be oxidized by the Mn(III)/(IV) in the nodule, following conversion of resulting Fe(III) to magnetite (Schaefer et al., 2017).

Another pathway of magnetite formation is the oxidation and precipitation of Fe(II), followed by further Fe(II)-induced transformation to magnetite. Hansel et al. (2003, 2005) proposed that a separate, ferrihydrite-generating step would be necessary in order to induce mineral "ripening" from goethite to magnetite. Similarly, ferrihydrite also appeared in the products using the Mössbauer characterization in the present study. The formed ferrihydrite were of significance for suggesting that after electron exchange between $Fe(II)_{(aq)}$ and $Fe(III)_{oxide}$, the resulting Fe(III) may be initially converted to the metastable ferrihydrite phase before to form the magnetite phase. The coexistence of the relatively large amount of $Fe(II)_{(aq)}$ with ferrihydrite could form magnetite as reported previously (Usman et al., 2012). In addition, both Mn(III) and Mn(IV) could serve as the oxidants, as in Eqs. (3a) and (3b), and therefore leading to a potential source of ferrihydrite in the magnetite formation process. The indirect magnetite formation process consists of three steps: formation of Fe(III) from Fe(II) (Eqs. (3a), (3b)) and precipitation of Fe(III) (Eq. (4)), followed by Fe(II)-induced transformation to magnetite (Eq. (5)). In Eqs. (4) and (5), $Fe(OH)_{3(s)}$ represents a simplified abstraction of ferrihydrite, formed from hydrolysis of Fe(III) in Eq. (4). Once magnetite is formed in the system, it can

subsequently grow with Fe(II) from solution, and Fe(III) from dissolution of nodule goethite.

Direct goethite transformation:

$$2FeOOH_{(s)} + Fe^{2+}{}_{(aq)} \rightarrow Fe_3O_{4(s)} + 2H^{+}{}_{(aq)} \quad (2)$$

Indirect path of magnetite formation, step 1:

$$2Fe^{2+}{}_{(aq)} + Mn(IV)_{(s)} \rightarrow 2Fe^{3+} + Mn(II) \quad (3a)$$

$$Fe^{2+}{}_{(aq)} + Mn(III)_{(s)} \rightarrow Fe^{3+} + Mn(II) \quad (3b)$$

Indirect path of magnetite formation, step 2:

$$Fe^{3+}{}_{(aq)} + 3OH^{-}{}_{(aq)} \rightarrow Fe(OH)_{3(s)} \quad (4)$$

Indirect path of magnetite formation, step 3:

$$2Fe(OH)_{3(s)} + Fe^{2+} \rightarrow Fe_3O_{4(s)} + 2\,H_2O_{(l)} + 2H^{+}{}_{(aq)} \quad (5)$$

## 5. Conclusions

In this study we observed Fe atom exchange between $Fe(II)_{(aq)}$ and $Fe(III)_{oxide}$ and Mn(III)/$Mn(IV)_{oxide}$ of ferromanganese nodule materials. Additionally, Fe(II)-induced phase transformation of the nodule resulted in the conversion of goethite to magnetite. Electron transfer and Fe atom exchange occurred between the sorbed $Fe(II)_{(aq)}$ and $Fe(III)_{oxide}$ as well as Mn(III)/$Mn(IV)_{oxide}$ in the nodule material, and the extent of Fe atom exchange increased at higher reaction pH. Concurrent with the electron transfer and Fe atom exchange between $Fe(II)_{(aq)}$ and the nodule, Fe(II)-induced formation of magnetite was observed, and within 30 days magnetite became the dominant mineral in the system (whereas goethite was dominant in the unreacted nodules). Two pathways are potentially responsible for the formation of magnetite. Firstly, due to the likely structural disorder of the goethite in the nodule, some crystalline goethite can be directly transformed to magnetite induced by $Fe(II)_{(aq)}$ (Jeon et al., 2001). Secondly, Mn(III) reduction occurred, suggesting that Fe(II) were oxidized by Mn to generate Fe(III) precipitates, which could have been induced by $Fe(II)_{(aq)}$ to form magnetite. In either of the two possible pathways, the coexistence of Mn oxides and other mineral components are necessary to make the transformation of goethite to magnetite possible.

## Declaration of competing interest

The authors declare that they have no known competing financial interests or personal relationships that could have appeared to influence the work reported in this paper.

## Acknowledgements

The authors sincerely thank Professor Michelle Scherer at the University of Iowa for the help in the experimental designs and discussions. Maxim Boyanov, Kenneth Kemner, and Bhoopesh Mishra are thanked for providing data collection support and Mn standards at the MRCAT/EnviroCAT beamline. This work was funded by the Natural Science Foundation of China (U1612442, U1701241 and 41673135), the Strategic Priority Research Programme of CAS (XDB40020000), the Science and Technology Foundation of Guangdong Province, China (2016TX03Z086, 2017BT01Z176 and 2017B030314092), the Innovation-driven Development Capability Construction Program of GDAS (2019GDASYL-0301002 and 2019GDASYL-0401003). MRCAT/EnviroCAT beamlines at the APS are supported by the U.S. Department of Energy and MRCAT/EnviroCAT member institutions.

## Appendix A. Supplementary data

Supplementary data to this article can be found online at https://doi.org/10.1016/j.chemgeo.2020.119901.

## References

Boland, D.D., Collins, R.N., Miller, C.J., Glover, C.J., Waite, T.D., 2014. Effect of solution and solid-phase conditions on the Fe(II)-accelerated transformation of ferrihydrite to lepidocrocite and goethite. Environ. Sci. Technol. 48, 5477–5485.
Borch, T., Kretzschmar, R., Kappler, A., 2010. Biogeochemical redox processes and their impact on contaminant dynamics. Environ. Sci. Technol. 44, 15–23.
Burton, E.D., Johnston, S.G., Watling, K., Bush, R.T., Keene, A.F., Sullivan, L.A., 2010. Arsenic effects and behavior in association with the Fe(II)-catalyzed transformation of schwertmannite. Environ. Sci. Technol. 44 (6), 2016–2021.
Casey, W.H., 2001. A view of reactions at mineral surfaces from the aqueous phase. Mineral. Mag. 65, 323–337.
Chang, C.Y., Li, F.B., Liu, C.S., Gao, J.F., Tong, H., Chen, M.J., 2016. Fractionation characteristics of rare earth elements (REEs) linked with secondary Fe, Mn, and Al minerals in soils. Acta Geochim 35, 329–339.
Chao, T.T., 1972. Selective Dissolution of manganese oxides from soils and sediments with acidified hydroxylamine hydrochloride. Soil Sci. Soc. Am. J. 36 (5), 764–769.
Chen, M.J., Liu, C.S., Li, F.B., Zhai, G.S., Liu, H., Liu, C.P., Yu, W.M., 2014. Correlations between soil geochemical properties and Fe(III) reduction suggest microbial reducibility of iron in different soils from Southern China. Catena 123, 176–187.
Cheng, W., Xu, J., Wang, Y., Zheng, W., Wu, F., Li, J., 2015. Synthesis of porous superparamagnetic iron oxides from colloidal nanoparticles: effect of calcination temperature and atmosphere. Mater. Chem. Phys. 153, 187–194.
Cismasu, A.C., Michel, F.M., Tcaciuc, A.P., Tyliszczak, T., Brown, G.G., 2011. Composition and structural aspects of naturally occurring ferrihydrite. Compt. Rendus Geosci. 343, 210–218.
Cornu, S., Deschatrettes, V., Salvador-Blanes, S., Clozel, B., Hardy, M., Branchut, S., Forestier, L.L., 2005. Trace element accumulation in Mn-Fe-oxide nodules of a planosolic horizon. Geoderma 125, 11–24.
Frierdich, A.J., Catalano, J.G., 2012a. Distribution and speciation of trace elements in iron and manganese oxide cave deposits. Geochim. Cosmochim. Acta 91, 240–253.
Frierdich, A.J., Catalano, J.G., 2012b. Controls on Fe(II)-activated trace element release from goethite and hematite. Environ. Sci. Technol. 46, 1519–1526.
Frierdich, A.J., Catalano, J.G., 2012c. Fe(II)-Mediated reduction and repartitioning of structurally incorporated Cu, Co, and Mn in iron oxides. Environ. Sci. Technol. 46 (20), 11070–11077.
Frierdich, A.J., Scherer, M.M., Bachman, J.E., Engelhard, M.H., Rapponotti, B.W., Catalano, J.G., 2012. Inhibition of trace elements release during Fe(II)-activated recrystallization of Al-, Cr-, and Sn-substituted goethite and hematite. Environ. Sci. Technol. 46, 10031–10039.
Frierdich, A.J., Beard, B.L., Reddy, T.R., Scherer, M.M., Johnson, C.M., 2014a. Iron isotope fractionation between aqueous Fe(II) and goethite revisited: New insight based on a multi-direction approach to equilibrium and isotopic exchange rage modification. Geochim. Cosmochim. Acta 137, 383–398.
Frierdich, A.J., Beard, B.L., Scherer, M.M., Johnson, C.M., 2014b. Determination of the $Fe(II)_{aq}$-magnetite equilibrium iron isotope fractionation factor using the three-isotope method and a multi-direction approach to equilibrium. Earth Planet. Sci. Lett. 391, 77–86.
Frierdich, A.J., Helgeson, M., Liu, C.S., Wang, C., Rosso, K.M., Scherer, M.M., 2015. Iron atom exchange between hematite and aqueous Fe(II). Environ. Sci. Technol. 49, 8479–8486.
Frierdich, A.J., Saxey, D.W., Adineh, V.R., Fougerouse, D., Reddy, S.M., Rickard, W.D.A., Sadek, A.Z., Southall, S.C., 2019. Direct observation of nanoparticulate goethite recrystallization by atom probe analysis of isotopic tracers. Environ. Sci. Technol. 53, 13126–13135.
Gorski, C.A., Handler, R.M., Beard, B.L., Pasakarnis, T., Johnson, C.M., Scherer, M.M., 2012. Fe atom exchange between aqueous $Fe^{2+}$ and magnetite. Environ. Sci. Technol. 46, 12399–12407.
Handler, R.M., Beard, B.L., Johnson, C.M., Scherer, M.M., 2009. Atom exchange between aqueous Fe(II) and goethite: an Fe isotope tracer study. Environ. Sci. Technol. 43, 1102–1107.
Handler, R.M., Frierdich, A.J., Johnson, C.M., Rosso, K.M., Beard, B.L., Wang, C., Latta, D.E., Neumann, A., Pasakarnis, T., Premaratne, W.A.P.J., Scherer, M.M., 2014. Fe(II)-catalyzed recrystallization of goethite revisited. Environ. Sci. Technol. 48, 11302–11311.
Hanna, K., Kone, T., Medjahdi, G., 2008. Synthesis of the mixed oxides of iron and quartz and their catalytic activities for the Fenton-like oxidation. Catal. Commun. 9, 955–959.
Hansel, C.M., Benner, S.G., Neiss, J., Dohnalkova, A., Kukkadapu, R.K., Fendorf, S., 2003. Secondary mineralization pathways induced by dissimilatory iron reduction of ferrihydrite under advective flow. Geochim. Cosmochim. Acta 67, 2977–2992.
Hansel, C., Benner, S.G., Fendorf, S., 2005. Competing Fe(II)-induced mineralization pathways of ferrihydrite. Environ. Sci. Technol. 39, 7147–7153.
Hansel, C., Learman, D., Lentini, C., Ekstrom, E., 2011. Effect of adsorbed and substituted Al on Fe(II)-induced mineralization pathways of ferrihydrite. Geochim. Cosmochim. Acta 75, 4653–4666.
Huang, L., Liu, F., Tan, W., Hu, H., Wang, M.K., 2009. Geochemical characteristics of

selected elements in iron-manganese cutans and matrices of Alfisols in Central China. J. Geochem. Explor. 103, 30–36.
Jeon, B.H., Dempsey, B.A., Burgos, W.D., Royer, R.A., 2001. Reactions of ferrous iron with hematite. Colloids Surf. A Physicochem. Eng. Asp. 191, 41–55.
Jien, S., Hseu, Z., Chen, Z., 2010. Hydropedological implications of ferromanganiferous nodules in rice-growing Plinthitic Ultisols under different moisture regimes. Soil Sci. Soc. Amer. 74, 880–891.
Jones, A.M., Collins, R.N., Rose, J., Waite, T.D., 2009. The effect of silica and natural organic matter on the Fe(II)-catalyzed transformation and reactivity of Fe(III) minerals. Geochim. Cosmochim. Acta 73, 4409–4422.
Jones, A.M., Collins, R.N., Waite, T.D., 2017. Redox characterization of the Fe(II)-catalyzed transformation of ferrihydrite to goethite. Geochim. Cosmochim. Acta 218, 257–272.
Joshi, P., Fantle, M.S., Larese-Casanova, P., Gorski, C.A., 2017. Susceptibility of goethite to $Fe^{2+}$-catalyzed recrystallization over time. Environ. Sci. Technol. 51, 11681–11691.
Kosmulski, M., 2001. Chemical Properties of Material Surfaces. CRC Press, New York.
Langlois, C.L., James, B.R., 2015. Chromium oxidation-reduction chemistry at soil horizon interfaces defined by iron and manganese oxides. Soil Sci. Soc. Am. J. 79 (5), 1329–1339.
Latta, D.E., Bachman, J.E., Scherer, M.M., 2012. Fe electron transfer and atom exchange in goethite: influence of Al-substitution and anion sorption. Environ. Sci. Technol. 46, 10614–10623.
Lindsay, W.L., 1979. Chemical Equilibriain Soils. Wiley-Interface.
Liu, C.S., Zhu, Z.K., Li, F.B., Liu, T.X., Liao, C.Z., Lee, J.J., Shih, K.M., Tao, L., Wu, Y.D., 2016. Fe(II)-induced phase transformation of ferrihydrite: the inhibition effects and stabilization of divalent metal cations. Chem. Geol. 444, 110–119.
Liu, C.S., Li, F.B., Chen, M.J., Liao, C.Z., Tong, H., Hua, J., 2017. Adsorption and stabilization of Lead during Fe(II)-catalyzed phase transformation of ferrihydrite. Acta Chim. Sin. 75, 621–628.
Lu, X.W., Shih, K., Liu, C.S., Wang, F., 2013. Extraction of metallic Lead from cathode ray tube (CRT) funnel glass by thermal reduction with metallic iron. Environ. Sci. Technol. 47, 9972–9978.
Manceau, A., Schlegel, M.L., Musso, M., Sole, V.A., Gauthier, C., Petit, P.E., Trolard, F., 2000. Crystal chemistry of trace elements in natural and synthetic goethite. Geochim. Cosmochim. Acta 64, 3643–3661.
Manceau, A., Tamura, N., Celestre, R.S., Macdowell, A.A., Geoffroy, N., Sposito, G., Padmore, H.A., 2003. Molecular scale speciation of Zn and Ni in soil ferromanganese nodules form Loess soils of the Mississippi basin. Environ. Sci. Technol. 37, 75–80.
Manceau, A., Lanson, M., Geoffroy, N., 2007. Natural speciation of Ni, Zn, Ba, and As in ferromanganese coatings on quartz using X-ray fluorescence, absorption, and diffraction. Geochim. Cosmochim. Acta 71, 95–128.
Marcus, M.A., Toner, B.M., Takahashi, Y., 2018. Forms and distribution of Ce in a ferromanganese nodule. Mar. Chem. 202, 58–66.
Massey, M.S., Lezama-Pacheco, J.S., Michel, F.M., Fendorf, S., 2014a. Uranium incorporation into aluminum-substituted ferrihydrite during iron(II)-induced transformation. Environ. Sci. Proc. Impacts 16, 2137–2144.
Massey, M.S., Lezama-Pacheco, J.S., Jones, M.E., Llton, E.S., Cerrato, J.M., Bargar, J.R., Fendorf, S., 2014b. Competing retention pathways of uranium upon reaction with Fe (II). Geochim. Cosmochim. Acta 142, 166–1852.
Masue-Slowey, Y., Loeppert, R.H., Fendorf, S., 2011. Alteration of ferrihydrite reductive dissolution and transformation by adsorbed As and structural Al: implications for As retention. Geochim. Cosmochim. Acta 75, 870–886.
Milad, K., Taymor, E., 2017. Integration of SEM/WDX elemental mapping and micromorphology to determine mineralogical traits of peat soils (case study: Northern Iran). Acta Geochim 36, 298–315.
Mohwinkel, D., Kleint, C., Koschinsky, A., 2014. Phase associations and potential selective extraction methods for selected high-tech metals from ferromanganese nodules and crusts with siderophores. Appl. Geochem. 43, 13–21.
Naskar, N., Lahiri, S., Chaudhuri, P., 2016. HF-free microwave assisted dissolution of soil samples for quantitative assessment of potassium. J. Indian Chem. Soc. 93, 799–803.
Neumann, A., Olson, T.L., Scherer, M.M., 2013. Spectroscopic evidence for Fe(II)-Fe(III) electron transfer at clay mineral edge and basal sites. Environ. Sci. Technol. 47, 6969–6977.
Neumann, A., Wu, L., Li, W., Beard, B.L., Johnson, C.M., Rosso, K.M., Frierdich, A.J., Scherer, M.M., 2015. Atom exchange between aqueous Fe(II) and structural Fe in clay minerals. Environ. Sci. Technol 49, 2786–2795.
Notini, L., Latta, D.E., Neumann, A., Pearce, C.I., Sassi, M., N'Diaye, A.T., Rosso, K.M., Scherer, M.M., 2018. The role of defects in Fe(II)-goethite electron transfer. Environ. Sci. Technol 52, 2751–2759.
Pedersen, H.D., Postma, D., Jakobsen, R., Larsen, O., 2005. Fast transformation of iron oxyhydroxides by the catalytic action of aqueous Fe(II). Geochim. Cosmochim. Acta 69, 3967–3977.
Ravel, á., Newville, M., 2005. ATHENA, ARTEMIS, HEPHAESTUS: data analysis for X-ray absorption spectroscopy using IFEFFIT. J. Synchrotron Radiat. 12, 537–541.
Reddy, T.R., Frierdich, A.J., Beard, B.L., Johnson, C.M., 2015. The effect of pH on stable iron isotope exchange and fractionation between aqueous Fe(II) and goethite. Chem. Geol. 397, 118–127.
Roden, E.E., 2012. Microbial iron-redox cycling in subsurface environments. Biochem. Society Trans. 40, 1249–1256.
Rosso, K.M., Yanina, S.V., Gorski, C.A., Larese-Casanova, P., Scherer, M.M., 2010. Connecting observations of hematite ($\alpha$-$Fe_2O_3$) growth catalyzed by Fe(II). Environ. Sci. Technol. 44, 61–67.
Schaefer, M.V., Handler, R.M., Scherer, M.M., 2017. Fe(II) reduction of pyrolusite (β-MnO2) and secondary mineral evolution. Geochem. T. 18 (7).
Schwertamnn, U., Cornell, R.M., 2000. Iron Oxides in the Laboratory: Preparation and Characterization, 2nd edition. Wiley-VCH, New York, USA.
Scroth, B.K., Sposito, G., 1997. Surface charge properties of kaolinite. Clay Clay Miner. 45, 85–91.
Stookey, L., 1970. Ferrozine: a new spectrophotometric reagent for iron. Anal. Chem. 42, 779–781.
Szymański, W., Skiba, M., Blachowski, A., 2014. Mineralogy of Fe-Mn nodules in Albeluvisols in the Carpathian Foothills, Poland. Geoderma 217, 102–110.
Tamaura, Y., Ito, K., Katsura, T.T., 1983. Transformation of γ-FeO(OH) to $Fe_3O_4$ by adsorption of iron(II) ion on γ-FeO(OH). J. Chem. Soc. Dalton Trans. 1983, 189–194.
Tan, W., Liu, F., Feng, X., Huang, Q., Li, X., 2005. Adsorption and redox reactions of heavy metals on Fe-Mn nodules from Chinese soils. J. Colloid Interf. Sci. 284, 600–605.
Taylor, S.D., Liu, J., Zhang, X., Arey, B.W., Kovarik, L., Schreiber, D.K., Perea, D.E., Rosso, K.M., 2019. Visualizing the iron atom exchange front in the Fe(II)-catalyzed recrystallization of goethite by atom probe tomography. Proc. Natl Acad. Sci. USA 116, 2866–2874.
ThomasArrigo, L.K., Mikutta, C., Byrne, J., Kappler, A., Kretzschmar, R., 2017. Iron(II)-catalyzed iron atom exchange and mineralogical changes in iron-rich organic freshwater flocs: an iron isotope tracer study. Environ. Sci. Technol. 51, 6897–6907.
Timofeeva, Y.O., 2008. Accumulation and fractionation of trace elements in soil ferromanganese nodules of different size. Geochem. Int. 46, 260–267.
Timofeeva, Y.O., Karabtsov, A.A., Semal, V.A., Burdukovskii, M.L., Bondarchuk, N.V., 2014. Iron-manganese nodules in udepts: the dependence of the accumulation of trace elements on nodule size. Soil Sci. Soc. Amer. 78, 767–778.
Tishchenko, V., Meile, C., Scherer, M.M., Pasakarnis, T.S., Thompson, A., 2015. $Fe^{2+}$ catalyzed iron atom exchange and re-crystallization in a tropical soil. Geochim. Cosmochim. Acta 148, 191–202.
Toby, B.H., 2001. EXPGUI, a graphical user interface for GSAS. J. Appl. Crystallogr. 34, 210–213.
Usman, M., Hanna, K., Abdelmoula, M., Zegeye, A., Faure, P., Ruby, C., 2012. Formation of green rust via mineralogical transformation of ferric oxides. Appl. Clay Sci. 64, 38–43.
Weber, K.A., Achenbach, L.A., Coates, J.D., 2006. Microorganisms pumping iron: anaerobic microbial iron oxidation and reduction. Nat. Rev. Microbiol. 4, 752–764.
Williams, A.G.B., Scherer, M.M., 2004. Spectroscopic evidence for Fe(II)-Fe(III) electron transfer at the Fe oxide-water interface. Environ. Sci. Technol. 38, 4782–4790.
Yang, L., Steefel, C.I., Marcus, M.A., Bargar, J.R., 2010. Kinetics of Fe(II)-catalyzed transformation of 6-line ferrihydrite under anaerobic flow conditions. Environ. Sci. Technol. 44, 5469–5475.
Yanina, S.V., Rosso, K.M., 2008. Linked reactivity at mineral-water interfaces through bulk crystal conduction. Science 320, 218–222.
Yu, X., Fu, Y., Brookes, P.C., Lu, S.G., 2015. Insights into the formation process and environmental fingerprints of iron-manganese nodules in subtropical soils of China. Soil Sci. Soc. Amer. J. 79, 1101–1114.
Zhou, Z., Latta, D.E., Noor, N., Thompson, A., Borch, T., Scherer, M.M., 2018. Fe(II)-catalyzed transformation of organic matter – ferrihydrite coprecipitates: a closer look using Fe isotopes. Environ. Sci. Technol. 52, 11142–11150.